Cerebellar acceleration of learning in an evidence-accumulation task

Marlies Oostland[1,†,*], Mikhail Kislin[1], Yuhang Chen[1], Tiffany Chen[2],

Sarah Jo Venditto[1], Ben Deverett[3], Samuel S.-H. Wang[1,*]

[1]Neuroscience Institute, Princeton University, Princeton, NJ, USA.

[2]Department of Neurological Surgery, University of California, San Francisco, CA, USA.

[3]Department of Anesthesiology, Stanford University Medical Center, Stanford, CA, USA.

[†]Present address: Wolfson Institute for Biomedical Research, University College London, London, UK.

*Correspondence: sswang@princeton.edu (SW), m.oostland@ucl.ac.uk (MO)

Abstract

Perturbation to the cerebellum can lead to motor dysfunction, cognitive deficits, and behavioral inflexibility. Here we report that a cerebellum-specific transgenic mouse model with disrupted Purkinje cell function shows unexpectedly accelerated learning on a sensory evidence-accumulation task, as well as enhanced sensory reactivity to touch and auditory cues. Computational latent-state analysis of behavior revealed that accelerated learning was associated with enhanced focus on current over past trials. Learning was also accelerated by providing cue-locked optogenetic stimulation of Purkinje cells, but unaffected by continuous optogenetic interference with Purkinje cell activity. Both transgenic and optogenetically-boosted mice showed prolonged electrophysiological activity in Purkinje-cell complex spikes and anterior cingulate cortex. We suggest that cerebellar activity may shape evidence-accumulation learning by enhancing task focus and neocortical processing of current experience.

Introduction

The cerebellum's roles extend beyond movement to include cognition, sensory processing, learning, and memory (Carta et al., 2019; Hatten, 2020; Heijden et al., 2021). Recent neuroimaging, clinical, and animal research provides evidence for a cerebellar role in social cognition and adaptive prediction (Frosch et al., 2022; Ito, 2006; Stoodley and Tsai, 2021), and in mice, cerebellar disruption can lead to deficits in attention, behavioral flexibility, and social interaction (Badura et al., 2018). Functional effects can be long-lasting, since early-life cerebellar injury in humans leads to autism spectrum disorder and other nonmotor disabilities (Garfinkle et al., 2020; Küper and Timmann, 2013; Limperopoulos et al., 2007; Tsai et al., 2018; Wang et al., 2014).

Here, we present evidence for enhanced function in cerebellum-specific functional perturbations. To examine alterations in task performance that emerge from abnormal cerebellar circuits, we examined *L7-Tsc1* mutants, a mouse model in which *tuberous sclerosis complex 1* is deleted specifically in cerebellar Purkinje cells (Kloth et al., 2015; Tsai et al., 2012), as well as acute optogenetic perturbations of cerebellar activity. Our findings indicate that the cerebellum regulates sensory reactivity at brainwide scale to regulate task persistence and learning.

Results

L7-Tsc1 mutant mice have moderately reduced numbers of Purkinje cells (Figure 1A,B), and surviving Purkinje cells show lower firing rates both *ex vivo* (Tsai et al., 2012) and *in vivo*, with reduced simple-spike and complex-spike rates in awake animals (Figure 1C). *L7-Tsc1* mutant mice show perseveration and deficits in gait and social interactions, as well as deficits in relatively simple motor learning on the accelerating rotarod (Kloth et al., 2015; Tsai et al., 2012). We found that mutant mice were slower to learn a separate delay tactile startle conditioning behavior (DTSC) (Yamada et al., 2019) (Figure 1D), a cerebellum-dependent form of associative sensorimotor conditioning (Chen et al., 2022).

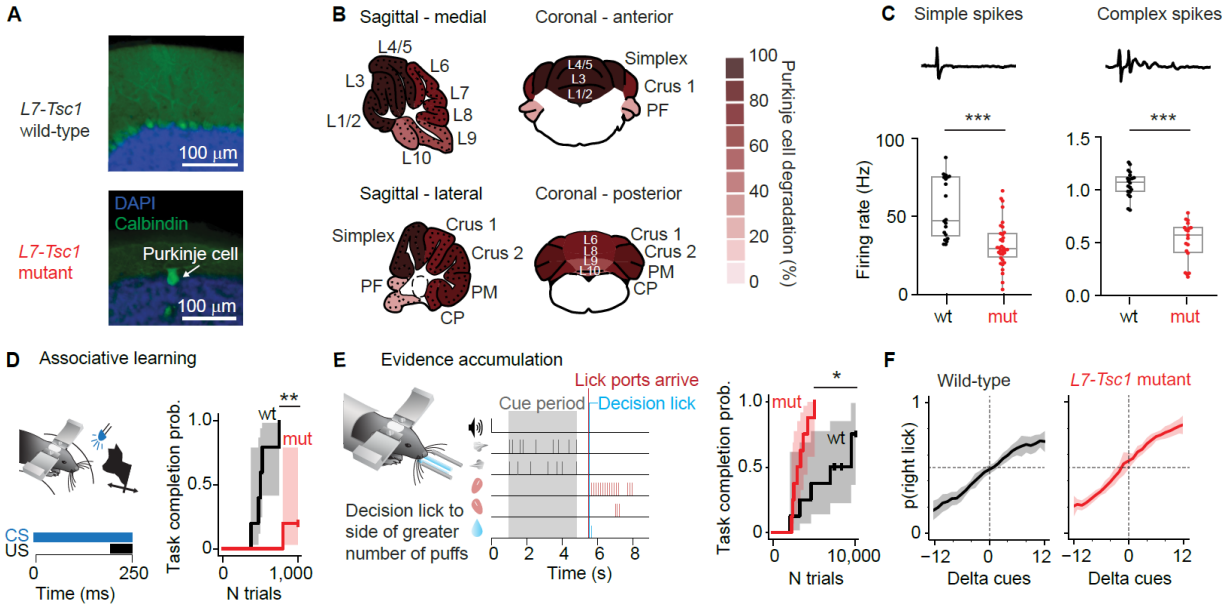

Figure 1 Cerebellar-impaired mice show enhanced learning of an evidence-accumulation decision-making task

(A) *L7-Tsc1* mutant mice have reduced number of Purkinje cells in the cerebellar cortex. (B) Schematic of sagittal and coronal views of the cerebellum with quantification of Purkinje cell loss averaged over 4 *L7-Tsc1* mutant mice at 5-6 months old for each cerebellar lobule, normalized to 3 wild-type littermates. (C) Reduced spontaneous *in vivo* firing rates of simple spikes and complex spikes in *L7-Tsc1* mutant mice (simple spikes: n = 34 cells, mean = 32 Hz, complex spikes: n = 19 cells from 4 mice, mean = 0.51 Hz) compared to wild-type littermates (simple spikes: n = 20 cells, mean = 55 Hz, $t(1) = 5.06$, $p = 5.5 \times 10^{-6}$, complex spikes: n = 20 cells from 5 mice, mean = 1.05 Hz, $t(1) = 10.55$, $p = 1.1 \times 10^{-12}$, both two-sided Student's t-tests). Example waveforms above each plot are 15 ms. (D) Impaired learning of the delayed tactile startle conditioning task for *L7-Tsc1* mutant mice (n = 5, median 1000 trials) compared to wild-type littermates (n = 5, median 500 trials, $\chi^2(1) = 9.70$, $p = 0.0018$, log-rank test). (E) Left: the evidence-accumulation task. Mice receive sensory airpuffs on the left and right whiskers, and receive a reward for correctly licking in the direction of more puffs. Right: Kaplan-Meier

estimator of probability of reaching the final level of task training for *L7-Tsc1* mutant mice (n = 8, median 3410 trials) and wild-type littermates (n = 8, median 9636 trials, $\chi^2(1) = 6.49$, p = 0.011, log-rank test). Shaded areas in Kaplan-Meier curves represent 95% confidence intervals. (F) Psychometric performance curves in mice who recently reached the final level show no detectable change in bias ($t(1) = 1.73$, $p = 0.21$), slope ($t(1) = 0.15$, $p = 0.70$), or lapse rate ($t(1) = 3.44$, $p = 0.085$, all two-sided Student's t-tests). Shading represents 1 s.d.

Enhanced learning and sensory responses

We examined more complex forms of learning and information processing by training mice to integrate sensory evidence in working memory using an established evidence-accumulation decision-making paradigm (Deverett et al., 2018; Pinto et al., 2018). Post-learning performance of this task depends on cerebellar crus I (Deverett et al., 2018, 2019), a region that is also necessary for other nonmotor functions (Badura et al., 2018) and where *L7-Tsc1* mutants have reductions in Purkinje cells (Figure 1B). During the task, mice receive sensory airpuffs on the left and right whiskers, and receive a reward for correctly licking in the direction of more puffs (Figure 1E). Mice progress through increasingly difficult levels of task shaping, during which evidence becomes more complex and an increasing temporal delay separates sensory information from the decision (Table S1).

We were surprised to find that *L7-Tsc1* mutant mice showed enhanced learning capabilities, successfully reaching the final level of training twice as quickly as wild-type littermates (Figure 1E). The faster learning rate was not correlated with sex, age, or corticosterone level. Faster learning already occurred at the earliest stages of training (Figure S1). Once animals had reached the expert stage, in the first few sessions at the final level there was no difference in overall performance between *L7-Tsc1* mutant mice and their wild-type littermates (Figure 1F; no significant difference in percentage correct trials: p=0.53, Welch's t-test, one-tailed; no significant difference in the slope parameter of the psychometric curve, p=0.31; no significant difference in the linear regression for slope for -5 to +5 range of cue difference, p=0.11). Mutant mice also did not differ from wildtypes in the number of licks per trial, either in correct trials (p=0.45, two-tailed t-test) or incorrect trials (p=0.23). Final performance is comparable to animals who have been trained extensively at the final level of a similar task (Deverett et al., 2018, 2019; Pinto et al., 2018).

Mutants stay on-task and in the present

To further explore the alterations in behavior associated with accelerated learning, we performed computational latent-state analysis of the learning process throughout training (Figure 2). Latent-state analysis identifies shifts in behavioral response patterns occurring between groups of trials that reveal variations in internal states over time (Ashwood et al., 2022; Bolkan et al., 2022; Calhoun et al., 2019). We fitted trial-by-trial outcomes to a generalized linear model - hidden Markov model (GLM-HMM, Figure 2A), trained on a separate data set of 22 wild-type mice and then fitted to the experimental animals (Figure 2B).

Based on these fits, mouse behavior could be sorted into three major categories that differed in their dependence on task parameters (Figure 2B). Mice in the on-task state 1 made the most correct decisions, relying heavily on the left-right difference in sensory cues, and less on the animals' choice in the previous trial. Early in training, wild-type mice tended to spend time in state 2, a past-trial-driven state in which mice relied more heavily on past rather than present information, thus reducing their decision accuracy, with responses strongly dependent on the choices made in the previous two trials; and state 3, an inattentive state in which mice were only weakly sensitive to any features of the task. On a moment-to-moment basis, wild-type mice made transitions from state to state on the time scale of dozens or hundreds of trials (Figure 2C). Each of these states had a distinct psychometric performance curve (Figure 2D) and dependency on past trials (Figure 2E) that were consistent with fit parameters. Within sessions, transitions away from state 1 occurred largely at the end of a session, when animals typically switched from the on-task state to the disengaged state (see example in Figure 2F).

Across sessions as training progressed, animals gradually shifted away from state 2 or 3 occupancy, eventually reaching consistent state 1 occupancy (Figure 2G,H,I). This shift in state occupancy occured in all animals, and took more trials for slower learners (examples in Figure 2G). To measure how this difference in occupancy evolved over training, we divided the behavioral data into two stages of task shaping: early, during which the animals still receive hint puffs to guide their choice, and late, during which animals need to accumulate the evidence in progressively more difficult trials. *L7-Tsc1* mutant mice already had higher state 1 occupancy than wild-type mice at the earliest stages of training, and this increased occupancy continued throughout the late stages (Figure 2I and Figure S1A). The shape of the psychometric curves of *L7-Tsc1* mutant mice in each state was similar to their wild-type littermates (Figure S2A,B).

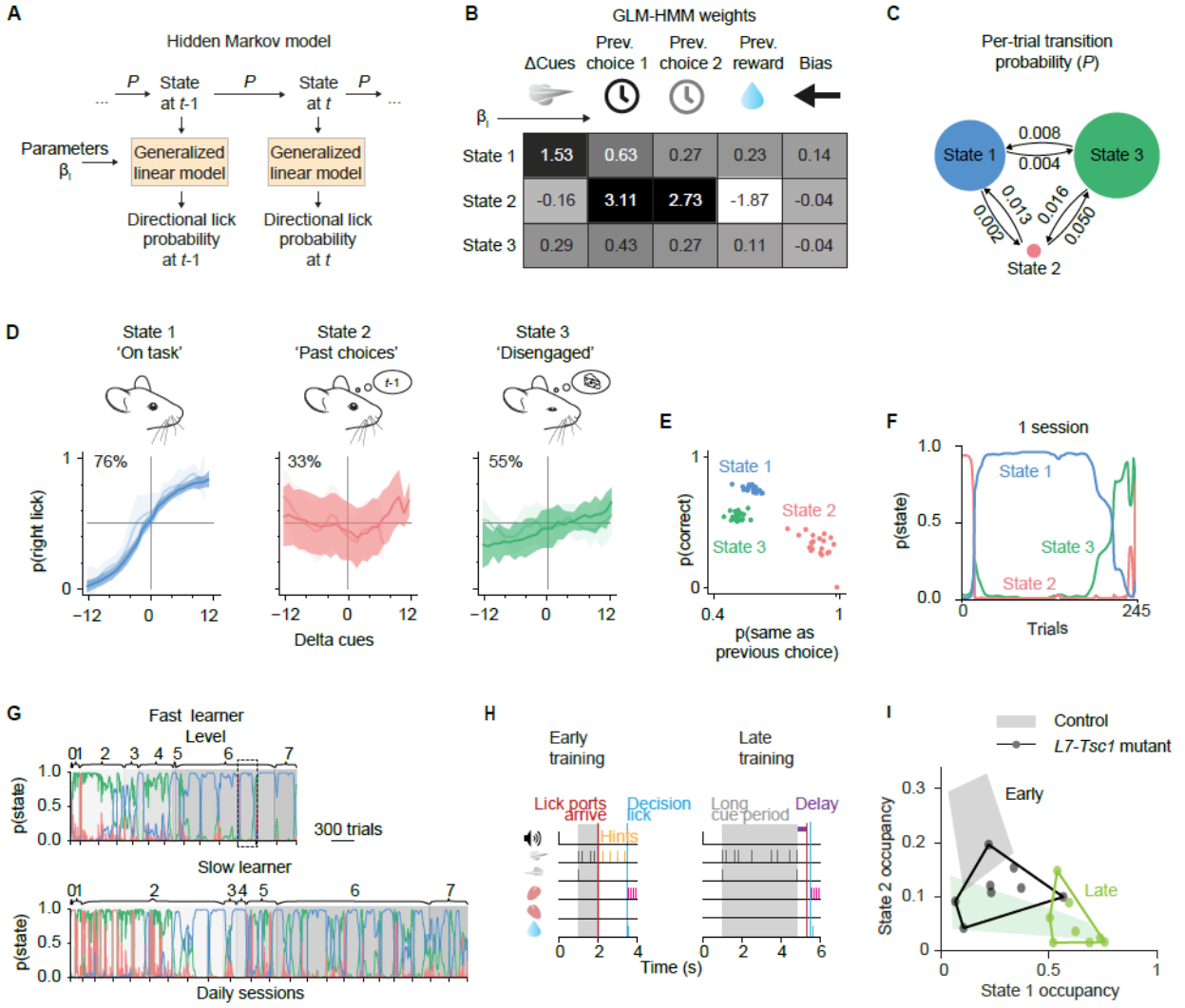

Figure 2 Latent behavioral-state analysis of task learning shows increased on-task focus in faster learners with cerebellar manipulations

(A) Schematic illustrating the GLM-HMM. *P* is state transition probability. (B) Inferred GLM-HMM weights from the training data set. (C) Per-trial transition rate between the three states averaged over all mice. The size of the circles indicate state occupancy across all trials of the mice in the training data set. (D) Psychometric curves averaged across all mice. In the top left is the percentage correct over all trials in that state. Shaded areas represent one s.d. Lighter curves indicate early trials and darker curves indicate late trials (see panel H). (E) Probability of a correct choice against the probability that the choice in the current trial was the same as the choice in the previous trial. Each data point represents the average across all trials for one mouse. (F) Posterior state probabilities for one example session. (G) Posterior state probabilities for all trials in all sessions from a fast learner (top) and a slow learner (bottom). The dashed area in the top panel indicates the session in F. (H) Two different stages of the evidence-accumulation task. (I) State 1 and state 2 occupancy during early and late stages for *L7-Tsc1* animals . Each data point represents one mouse. Shaded areas indicate the area covered by control animals.

Enhanced sensory reactivity is accompanied by increased neocortical response

Because simple associative conditioning was not improved in *L7-Tsc1* mice and because evidence-accumulation learning was faster even at the onset of training, we hypothesized that the accelerated learning rate might be related to specific processing steps that come subsequent to airpuff presentation. We therefore measured sensory reactivity before training. Naive *L7-Tsc1* mutant mice showed enhanced blink responses to individual airpuffs (Figure 3A), as well as to auditory stimuli (Figure S3A,B), indicative of altered sensory processing. In wild-type C57BL/6J mice, increasing the intensity of airpuffs from 10 psi to 20 psi was sufficient to accelerate training to a degree similar to that seen in *L7-Tsc1* mutant mice (Figure 3B), and increased the degree of state-1 occupancy in the earliest stages of training at which the puff intensity increase occurred, but not without any perturbation (Figure 3C, Figure S4A,B and Figure S1C). This suggests that pre-existing sensory reactivity may aid in high-accuracy performance during learning of a task requiring integration of sensory evidence, such as the evidence-accumulation task.

To measure neural signals accompanying enhanced sensory responsiveness, we performed *in vivo* electrophysiological recordings in crus I in naive mice (Figure 3D), a time when improved learning was already evident at early stages of training. In wild-type mice, sensory cues triggered complex spikes (Figure 3E,F), with a delayed simple-spike response (Figure 3G). In contrast, in *L7-Tsc1* mutant mice, complex spikes were activated only after a delay of several hundred milliseconds (Figure 3F), with decreased simple-spike response (Figure 3G) and the consequent expected disinhibition of negative feedback from deep nuclei (Figure S5A) onto inferior olivary neurons (Kim et al., 2020; Llinas, 2014).

Influences of cerebellum may be conveyed via long-range connections that project throughout thalamus and neocortex (Pisano et al., 2021), including two associative regions implicated in decision-making (Chabrol et al., 2019; Gao et al., 2018; Kennerley et al., 2006) that receive substantial disynaptic input from crus I (Pisano et al., 2021): anterior cingulate (Figure 3H) and anterolateral motor cortex (Figure S5B). Recordings from these regions showed an enhancement in cue-evoked activity with a similar time course as complex-spike activity. These effects were not seen in the barrel field of the primary somatosensory cortex (Figure S5C). These results suggest that cerebellar neural activity might play a causal role in influencing neocortical activity to drive learning.

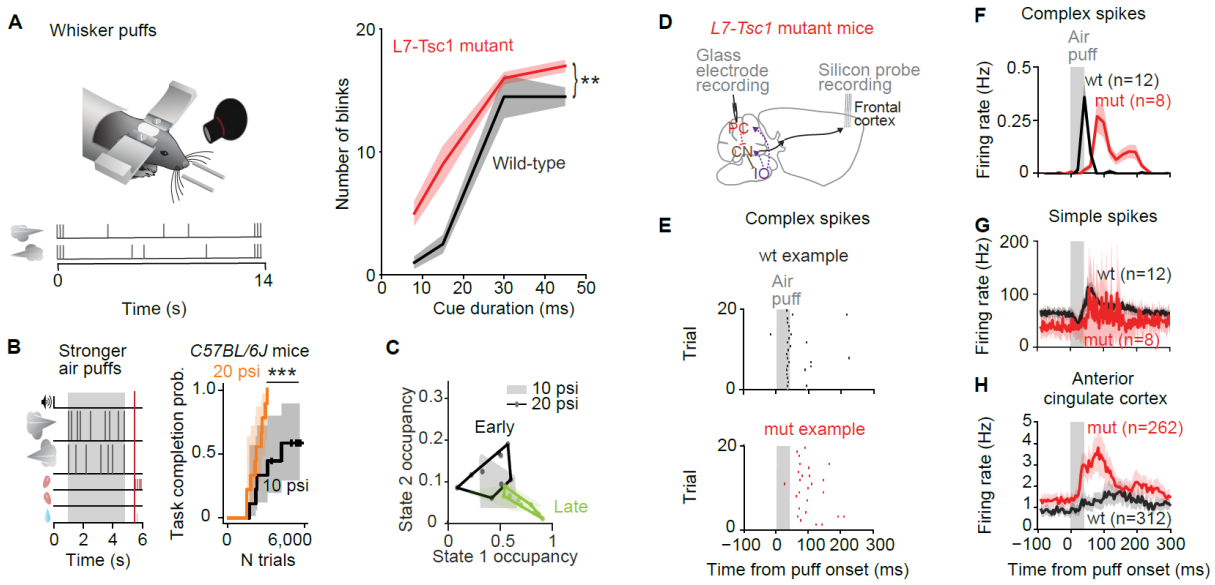

Figure 3 Prolonged whisker puff responses in awake behaving *L7-Tsc1* mice in cerebellar complex spikes and forebrain

(A) Left: schematic of sensory sensitivity test with bilateral and unilateral whisker puffs. Right: median number of eye blinks in response to whisker puffs of different durations for *L7-Tsc1* mutant mice (n = 16) and wild-type littermates (n = 7). A two-way ANOVA indicates an effect of genotype (F = 7.44, p = 0.008), as well as whisker puff duration (F = 32.80, $p = 3.9 \times 10^{-14}$), but no interaction effect (F = 0.98, p = 0.4). Shaded areas indicate the estimated s.e.m. using median absolute deviation. (B) Increased sensory salience through stronger puffs also leads to enhanced learning. Kaplan-Meier estimator of task completion for C57BL/6J animals receiving standard (10 psi, n = 9, median 4275 trials) or stronger (20 psi, n = 9, median 2225 trials) whisker puffs during the evidence accumulation task ($\chi^2(1) = 7.11$ p = 0.00047, log-rank test). Shaded areas in Kaplan-Meier curves represent 95% confidence intervals. (C) State 1 and state 2 occupancy during early and late stages for mice with standard or stronger whisker puffs. Each data point represents one mouse. Shaded areas indicate the area covered by control animals. (D) Recording sites in cerebellum-neocortical path of influence in whisker puff responses in *L7-Tsc1* mutant mice. (E) Example raster plots of Purkinje cell complex spikes during 20 trials from one wild-type animal (top) and one *L7-Tsc1* mutant animal (bottom). (F-H) Average firing rates in response to an air puff to the whiskers (data from 4 *L7-Tsc1* mutants and 5 wild-type mice) for Purkinje cell complex spikes (F), Purkinje cell simple spikes (G) and for anterior cingulate cortex (H). Shaded areas represent 95% confidence intervals.

Optogenetic replication of fast learning

In *L7-Tsc1* mutant mice, Purkinje cell function is altered chronically. To determine whether enhanced learning could arise from acute perturbation, we directly manipulated neural activity in wild-type mice by expressing the optogenetic probe channelrhodopsin-2 in Purkinje cells (Figure 4). We optogenetically reinforced each cue, starting after mice had passed out of the early stage of training, by pairing each sensory stimulus with an ipsilateral light flash (cue-locked "opto-boosting") applied over crus I (Figure 4A). Opto-boosting led to faster learning than in controls not expressing ChR2 (Figure 4A). Furthermore, mice showed an immediate tendency toward increased occupancy of on-task state 1 and reduced occupancy of prior-trial state 2 (Figure S1B). Specifically, 4 out of 5 optogenetically-reinforced mice spent more than 90% of the trials in state 1 and fewer than 5% of the trials in state 2 (Figure 4B). This tendency continued all the way through late training.

Cerebellum-driven acceleration of learning might arise from enhancement of immediate cue experience, or alternately require longitudinal shaping across sessions. Opto-boosting did not increase the number of blinks produced to individual airpuffs in a sensory reactivity test (within-mouse comparison; 25 psi puffs of 8-45 ms duration, $F(2,48)=0.23$, $p=0.80$ for opto-boosting vs. no boosting, linear mixed-effect model, 5 mice), consistent with a mechanism in which Purkinje cell simple-spike suppression, which is required for eyelid closure (Romano et al., 2018), occurs in *L7-Tsc1* mutant mice but not with opto-boosting. The amount of per-puff whisker movement in the evidence-accumulation task was also not affected by optogenetic boosting (Figure 4C, rise: $p=0.27$, decay: $p=0.53$, two-tailed Welch's *t*-test, $n=5$ ChR- mice and $n=6$ ChR+ mice), indicating that the accelerated learning which occurs both in the *L7-Tsc1* mutant mice and with optogenetic boosting does not covary with immediate sensorimotor processing.

In trained mice, when Purkinje cells in crus I are optogenetically stimulated continuously during the entire cue period and delay period including the first lick (Figure S6A), performance is impaired by forgetting immediately-past experience (Deverett et al., 2019). However, the amount of per-puff whisker movement in the evidence-accumulation task was not affected (Figure S6D, rise: $p=0.61$, decay: $p=0.33$, two-tailed Welch's *t*-test, $n=5$ ChR- mice and $n=6$ ChR+ mice). Even though such continuous stimulation increased overall simple-spike activity, it did not enhance simple-spike responses to individual sensory cues, and there was no change in complex spike firing in response to whisker puffs (Figure S6E,F) and no detectable effect on the learning rate (Figure

S6B) or whisker puff responses in forebrain areas (Figure S6G,I,J). At levels with optogenetic stimulation, there was no change in state 1 occupancy, although there was a reduction in state 2 occupancy (Figure S6C and Figure S1D). Thus, under all conditions that accelerated learning, reduction in state-2 occupancy was visible at the earliest stages of perturbation (Figure S1).

After training, optogenetic stimuli delivered without sensory cues could also drive decision-making above chance (Figure 4D), suggesting that alterations in Purkinje cell activity could target effectors in common with sensory cues. Thus learning can be augmented by boosting Purkinje cell activity during sensory stimulation, either via Tsc1 knockout or by optogenetic activation, both of which generate similar alterations of complex spike timing and neocortical activity.

Behavioral results were consistent with the similarity in complex spike and neocortical activity patterns compared to *L7-Tsc1* mutant mice. *In vivo* recordings in awake behaving naive ChR2-expressing mice (Figure 4E) indeed showed an increase in simple-spike firing during the air puff paired with optogenetic boosting (Figure 4H), the opposite of the effect seen in *L7-Tsc1* mutant mice. On the other hand, complex spike firing was increased and delayed (Figure 4F,G), a similar effect to that seen in *L7-Tsc1* mutant mice, due to a putatively disinhibitory effect of simple-spike firing on nucleo-olivary paths (Bengtsson and Hesslow, 2006). Firing enhancement coincided with the end of the optogenetic stimulus (Figure S7), consistent with a disinhibitory effect. Furthermore, silicon probe recordings in neocortex showed enhancements in associative anterior cingulate (Figure 4I) and anterolateral motor region (Figure S7B) activity, but not in the barrel field of the primary somatosensory cortex (Figure S7C), mimicking neocortical activity in *L7-Tsc1* mutant mice.

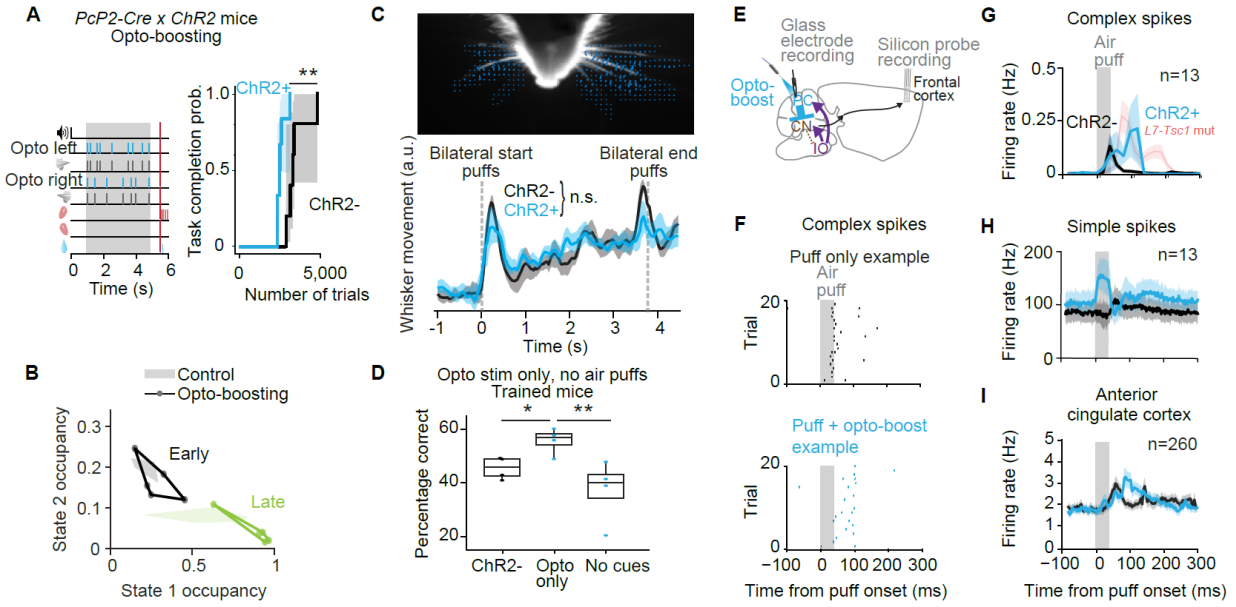

Figure 4 Altered whisker puff responses and faster learning with cue-locked optogenetic boosting of Purkinje cells

(A) Schematic and Kaplan-Meier estimator of task completion probability for *Pcp2-Cre* × *ChR2* mice with cue-locked bilateral optogenetic activation of crus I in the evidence-accumulation task (n = 6, median 2512 trials) and wild-type littermates (n = 5, median 3311 trials, $\chi^2(1) = 8.18$, p = 0.0042, log-rank test). (B) State 1 and state 2 occupancy during early and late stages for mice with or without opto-boosting of whisker puffs. Each data point represents one mouse. Shaded areas indicate the area covered by control animals. (C) Detection of whisker movement during the evidence-accumulation task in response to bilateral whisker puffs at the start and end of each trial. Blue arrows in the top plot indicate detection of whisker movement measured using a region-of-interest optical flow analysis. Shaded areas in the bottom plot include 95% confidence intervals. (D) Performance in the evidence-accumulation task in trained *Pcp2-Cre* × *ChR2* mice with only cue-locked optogenetic activation of Purkinje cells in crus I (n = 4, mean percentage correct: 55.8%), and two controls without stimuli: one without ChR2 expression (n = 4, 45.6% correct), the other without light (n = 4, 37.2% correct). Overall effect: $H(2) = 7.65$, p = 0.022 (Kruskal-Wallis test), with significant differences between ChR2+ and ChR2- mice (p = 0.046, Conover post-hoc test) and ChR2+ and no cues (p = 0.0044). Due to anti-biasing parameters, chance level different for each animal but always below 50%. (E) Recording sites in cerebellum-neocortical path of influence in whisker puff responses paired with optogenetic boosting of Purkinje cells in crus I. (F) Example raster plots of Purkinje cell complex spikes during 20 trials with only a whisker puff (top) or with a whisker puff paired with optogenetic stimulation (bottom). (G-I) Average firing rates in response to an air puff to the whiskers for Purkinje cell complex spikes (G, data from 4 mice), Purkinje cell simple spikes (H, data from same 4 mice) and for anterior cingulate cortex (I, data from 3 mice). The red line in G indicates the firing rate for *L7-Tsc1* mutant mice (Figure 3F) for comparison. Shaded areas represent 95% confidence intervals.

Discussion

Our experiments support the idea that cerebellar complex-spike output can accelerate nonmotor learning through increased on-task focus. Cerebellar activity is transmitted to neocortical structures via major paths through thalamus and other midbrain structures (Fujita et al., 2020; Pisano et al., 2021) that may convey these influences. Among the extensive neocortical targets of cerebellar projections is the parietal cortex, where, interestingly, silencing of activity was recently shown to improve performance in evidence accumulation by reducing reliance on past evidence (Akrami et al., 2018). Cerebellum and neocortex project to one another bidirectionally in a loopwise manner via thalamus, pons, and midbrain structures (Strick et al., 2009; Wagner and Luo, 2020), including distributed influence of lobules over diverse associative and premotor regions (Pisano et al., 2021). Such connectivity provides a substrate for delayed activation and spatially distributed responses. Indeed, in *L7-Tsc1* mutant mice, inhibition of the medial prefrontal cortex has previously been found to improve social deficits and repetitive behaviors (Kelly et al., 2020). In addition, it has recently been found that transcranial direct current stimulation of the right lateral posterior cerebellum improved performance on a sentence completion task, as well as altering activity in multiple neocortical regions (Rice et al., 2021).

The cerebellum and global coherence

The convergence of impaired associative motor learning, increased sensory sensitivity, and accelerated task learning through increased task focus (Figure 5) echoes traits found in autism spectrum disorder (ASD). ASD is associated with islands of enhanced function, including perceptual domains and technical or even artistic capacities (Happé and Frith, 2006; Mottron et al., 2006). According to the weak central coherence account of ASD, these enhanced capacities can be explained by a detail-focused cognitive style in which individual perceptual features are emphasized. In the global coherence account of autism spectrum disorder, the capacity to extract global form and meaning is displaced by superiority on local or detail-focused processing (Happé and Frith, 2006). Our findings with cerebellar perturbations demonstrate one aspect of such processing, sensory hypersensitivity (Mottron et al., 2006), and an association with accelerated capacity to learn a sensory-integration task. Our results also show one predicted feature of such increased sensitivity, hyperreactivity of neocortical circuits (Markram and Markram, 2010). The atypicalities of sensation and perception reported in ASD can be interpreted in terms of a

broadening of Bayesian priors about the sensory world. "Hypo-priors" can account for a tendency among autistic persons "to perceive the world more accurately rather than [be] modulated by prior experience" (Pellicano and Burr, 2012). Cerebellar disruption provides one neural substrate for hypo-prior formation, providing a substrate for a seemingly paradoxical phenomenon seen in ASD: broad disruption of cognitive and social function, accompanied by high performance in specific skill domains (Happé and Frith, 2006).

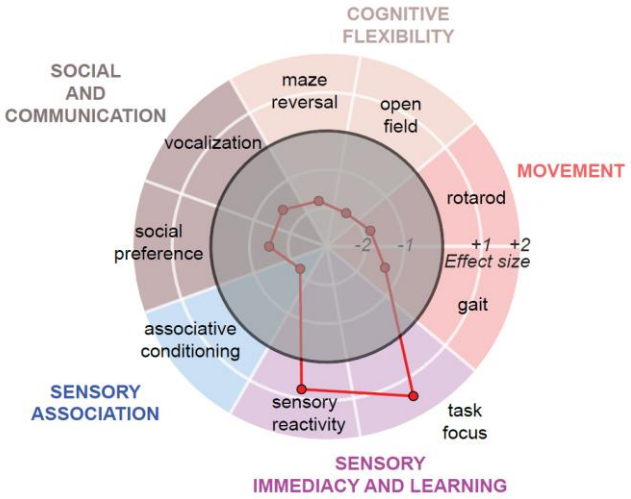

Figure 5 *L7-Tsc1* mutant mice express an island of enhanced sensory reactivity and task focus amid a variety of impairments

Each dot represents an estimated effect size (Cohen's *d*) for the behavior of *L7-Tsc1* mutant mice compared to their wild-type littermates. The thick circle indicates typical behavior (effect size 0). Based on data presented in this paper and from Tsai et al. 2012; Kloth et al. 2015; Klibaite et al. 2022.

Acknowledgements

We thank members of the Wang lab, the BRAIN CoGS consortium, and Michael Häusser for discussion and advice, G. Joseph Broussard, Caroline Jung, Junuk Lee, Laura Lynch, Dafina Pacuku, and John Wuethrich for help with experiments, Jonathan Pillow for advice on latent-state analysis, Zahra Dhanerawala, Austin Hoag, and Sanjeev Janarthanan from the BRAIN CoGS Histology Core for brain clearing, imaging and probe localization, and Carlos Brody, Sabine Kastner, Manuel Schottdorf and Thomas Zhihao Luo for comments on the manuscript. The work was supported by National Institutes of Health grants R01 NS045193, R01 MH115750, and U19 NS104648 to SW, and European Union's Horizon 2020 research and innovation programme under the Marie Skłodowska-Curie grant agreement No 844318 to MO.

Author contributions

S.W. and M.O. conceptualized the research. M.O., S.W., M.K. and B.D. designed the experiments. M.O., M.K. and T.C. performed the experiments. M.O. and Y.C. did data analysis and visualization. S.J.V. provided the code for the GLM-HMM analysis. M.O. and S.W. did funding acquisition, project administration, and supervision. S.W. and M.O. wrote the original draft, and M.O. and B.D. reviewed and edited the paper.

Declaration of interests

Authors declare no competing interests.

Methods

Mice. Experimental procedures were approved by the Princeton University Institutional Animal Care and Use Committee (protocol 1943-19) and performed in accordance with the animal welfare guidelines of the National Institutes of Health and in line with the European Directive 2010/63/EU on the protection of animals used for experimental purposes.

Data came from 133 mice (males and females, 2-5 months of age at the start of experiments) of genotypes C57BL/6J (The Jackson Laboratory, Bar Harbor, ME, 40 animals), *Pcp2-Cre* for Purkinje-cell specificity and *Ai27D* for channelrhodopsin-2 (33 animals *Pcp2-Cre* × *Ai27D*, acquired from The Jackson Laboratory, stock #010536 (RRID:IMSR_JAX:010536) and #012567 (RRID:IMSR_JAX:012567), respectively) and $L7^{Cre}$;$Tsc1^{flox/flox}$ mice (60 animals). To create these Purkinje cell specific $L7^{Cre}$;$Tsc1^{flox/flox}$ mice, $Tsc1^{flox/flox}$ ($Tsc1^{tm1Djk}$/J, The Jackson Laboratory stock #005680) mutant mice were crossed into L7-Cre mice (B6.129-Tg(Pcp2-cre)2Mpin/J, The Jackson Laboratory, stock #004146). Experimenters were blinded to the genotypes of the mice for the duration of the behavioral experiments.

All mice were group-housed in reverse light cycle to promote maximal performance during behavioral testing, which took time during the day. For long-term behavioral experiments, mice were housed in darkness in an enrichment box containing bedding, houses, wheels (Igloo and Fast-Trac; K3250/K3251; Bio-Serv; Flemington, NJ, USA), climbing chains, and play tubes during all experimental days. At other times, mice were housed in cages in the animal facility, in groups of 2–4 mice per cage. During experiments in which water intake was restricted, mice received 1.0–1.5 mL of filtered water per day plus half of a mini yogurt drop (F7577; Bio-Serv; Flemington, NJ, USA), and body weight and condition was monitored daily. Mice always had *ad libitum* access to food pellets.

Surgical procedures. For all surgeries, mice were anesthetized with isoflurane (5% for induction, 1.0–2.5% for maintenance), and were given buprenorphine (0.1 mg/kg body weight) and rimadyl (5 mg/kg body weight) after surgery and were given at least 5 days of recovery in their home cages before the start of experiments, except for acute *in vivo* electrophysiology experiments when the animals were allowed to recover for at least two hours between the craniotomy and the acute recordings.

For optogenetic experiments, a custom-machined titanium headplate (Dombeck et al., 2007) was cemented to the skull using dental cement (C and B Metabond, Parkell Inc.). Two ~500 μm diameter craniotomies were drilled over the cerebellum, one over each hemisphere, directly posterior to the lamboid suture and ~3.6mm lateral to the midline in either direction. Ferrule implants were constructed with 400-μm-diameter optical fiber (Thorlabs FT400EMT) glued to 1.25-mm OD stainless steel ferrules (Precision Fiber Products MM-FER2007-304-4500) using epoxy (Precision Fiber Products PFP 353ND). Ferrules were positioned over each craniotomy with the fiber tip at the surface of the dura mater, and Vetbond (3 M) was applied surrounding the exposed fiber. Dental cement was then applied to secure the ferrule to the skull. Implants were cleaned before each behavior session using a fiber optic cleaning kit (Thorlabs CKF).

For *in vivo* electrophysiology, a headplate was implanted as described above, and a 2 mm craniotomy was drilled over the area of interest and the dura removed. For recordings from neocortex, the following stereotaxic coordinates were used: anterior cingulate cortex: ML 0-0.5 mm, AP 0.5-1.5 mm, DV 0.7-1.0 mm, anterolateral motor cortex: ML 1.5 mm, AP 2.5 mm, DV 0.7-1.0 mm, and barrel field of the primary somatosensory cortex: ML 2.5 - 3.5 mm, AP -0.8 - -1.8 mm, DV 0.6-1.5 mm. Two stainless steel screws for ground and reference wires (000–120 1/16 SL bind machine screws, Antrin Miniature Specialties) were inserted in the skull above the forebrain as far away from the craniotomy as possible. For cerebellar recordings, a small hole was drilled for a reference electrode in the interparietal bone at the midline. Craniotomies (0.5 mm by 1–1.5 mm) were made next to intersection of interparietal and occipital bones and over the left and right lobule V and simplex for extracellular single-unit recordings. Craniotomies were covered with Kwik-Cast silicone adhesive (World Precision Instruments) until the time of the recording.

Behavior experiments. Mice were trained to perform an evidence-accumulation decision-making task as described previously (Deverett et al., 2018; 2019). The behavioral apparatuses were controlled by custom-written Python software as published previously (Deverett et al., 2018) (https://github.com/wanglabprinceton/accumulating_puffs). Animals were trained for 1.5-9.0 weeks, 7 days/week. Briefly, head-fixed mice were seated in a tube for daily 1 h behavioral sessions consisting of 200-300 trials. In each trial, independent streams of randomly timed 40 ms air puffs of 10 psi (unless otherwise indicated) with a minimum 200 ms interpuff interval were delivered to the left and right sides over the course of a 1.0-3.8-second cue period. After a delay

period of 200-800 ms, lick ports were advanced into the reach of the animal, and animals received a 4 µl water reward when they licked to the side with the greater number of puffs. The animal's decision was interpreted as the side licked first, regardless of subsequent licks. Anti-biasing procedures (Deverett et al., 2018) result in chance levels being <50%. To increase motivation, restriction of water intake started at least 5 days before the start of training and continued throughout the whole training period.

Animals went through different levels of training (levels 0-6) to reach the final version of the task (level 7). Mice automatically proceeded to the next level once they reached pre-defined performance criteria (see Table S1 for details of each level as well as the performance criteria). The time it took an animal to learn the task was defined as the total number of trials to reach level 7. Psychometric curves were fitted with the psychofit module (https://github.com/cortex-lab/psychofit).

Light for optogenetic stimulation during the evidence-accumulation task was delivered as described previously (Deverett et al., 2019). Cue-locked optogenetic activation occurred unilaterally, at the same side and time at an air puff, for a duration of 40 ms (generated by Master-8, A.M.P.I.). Continuous optogenetic activation occurred bilaterally with 5-ms pulses at 50 Hz throughout the entire cue period, delay period, and ended upon first lick contact. When optogenetic activation was used to manipulate the learning rate, the optogenetic activation only started from level 3, and at every trial from then on. When optogenetic activation was used to manipulate performance in trained mice, light was on in 20% of trials. In this case, analysis compares light-off and light-on trials only from behavioral sessions in which light was delivered.

For the delay tactile startle conditioning (DTSC) task (Yamada et al., 2019), mice learned to elicit a startle (backward) movement in response to an initially neutral conditioned stimulus (CS; 250 ms; 5mm 395-400nm UV Ultraviolet LED, EDGELEC) that was paired with a startle-eliciting unconditioned stimulus (US, 20 ms tactile stimulus on the nose by taping foam that was attached to the stepper motor shaft (High Torque Nema 17 Bipolar Stepper Motor 92oz.in/65Ncm 2.1A Extruder Motor, Stepper Online); CS-US inter-stimulus interval, 200 ms).

For sensory sensitivity tests, naive animals were headfixed in a similar setup to the evidence-accumulation setup and received either whisker puffs or auditory cues. Animals were not trained nor expected to do anything in response to the sensory cues, and did not receive any rewards throughout the session. Animals received cues in sequences of in total 24 cues starting and ending

with three cues with 200 ms inter-cue interval, and in between those, cues at random intervals (ranging from 0.8 to 3.0 s). Animals first received a sequence with cue durations of 8 ms, followed by sequences with longer cue durations (15, 30, and 45 ms for whisker puffs, and 15, 30, 45, 90, 180, 320, and 640 ms for auditory cues). Animals either received bilateral air puffs to the whiskers at 20-25 psi, or auditory cues at 12 kHz. During sensitivity tests with whisker puffs, white noise was on in the background throughout the experiment. To determine eye blink responses, movies of the right side of their face and body were acquired using two USB cameras (Playstation Eye), modified by removal of infrared filters and encasings. Images were acquired at 30 Hz with 320 × 240 pixel resolution. Illumination was provided by an infrared LED array (Yr.seasons 48-LED Illuminator Light CCTV 850 nm IR Infrared Night Vision). Air puffs were produced by activation of solenoids (NResearch, standard two-way normally closed isolation valve, 161T011) with input from an air source (ControlAir Type 850 Miniature Air Pressure Regulator). Air was delivered via two tubes custom-machined with uniform openings, and positioned parallel to one another, parallel to the anteroposterior axis of the animal, 10 mm apart mediolaterally and ~1 mm anterior to the nose of the animal. Auditory cues were delivered to the apparatus by a speaker (Sony Tweeter XS-H20S) mounted below the apparatus. Analysis of eye blinks was performed using FaceMap (https://github.com/MouseLand/facemap) with manual curation and further analysis in Python.

***In vivo* electrophysiology.** For acute recordings from awake behaving mice, animals were head-fixed over a freely rotating cylindrical treadmill and the craniotomy site was opened by removing the Kwik-Cast plug and then filled with saline. Recordings were performed using either silicon probes for neocortex or glass electrodes for cerebellum, as described below. Air puffs to the whiskers were delivered by a pressure injector system (Toohey Spritzer, Toohey, Fairfield, NJ, USA) which received signals from a signal generator (Master-8; AMPI) with an intensity of 20 psi and a frequency of 1 Hz, except for experiments with continuous optogenetic activation throughout the entire cue and delay period, when air puffs were delivered with a frequency of 0.2 Hz. Mice received unilateral air puffs ipsilaterally to the recording site for Purkinje cells, anterior cingulate cortex, and anterolateral motor cortex, and contralaterally to the recording site for cerebellar nuclei and the barrel field of the somatosensory cortex. For recordings with optogenetic stimulation, light onset started at the same time as the air puff for the duration of the air puff (40 ms) unless indicated

otherwise. In a subset of experiments (Figure S6D) light started at the same time as the air puff but remained on for longer (250 ms).

For neocortical recordings, a 64-channel silicon probe (Neuronexus, A4x16-5mm-50-200-177 or A2x32-Poly5-10mm-20s-200-100) covered in Vybrant™ CM-DiI Cell-Labeling Solution (V22888; Invitrogen) was slowly placed above the craniotomy and lowered into the brain using a motorized micromanipulator (MP-225; Sutter Instrument Co.). The silicon probes were connected to two amplifier boards (RHD2132, Intan Technologies) using a dual headstage adapter (RHD2000, Intan Technologies). Recordings were made using an Open Ephys acquisition board at a sampling rate of 30 kHz. High-pass filtering of the raw data at 300 Hz, common median referencing, and automatic spike sorting was achieved using Kilosort 2 (Pachitariu et al., 2016; https://github.com/cortex-lab/Kilosort). Spikes were further manually curated using the Phy GUI (https://github.com/kwikteam/phy).

Single-unit recordings of Purkinje neurons and cerebellar nuclei neurons were performed using borosilicate glass electrodes (1B100F-4, World Precision Instruments) with 1- to 2-µm tips, short for Purkinje cells or very long gradual tapers for cerebellar nuclei cells, and 3 to 12 MΩ impedance, fabricated on a pipette puller (P-2000, Sutter Instruments Co.) and filled with sterile saline. The electrode was lowered into the cerebellum using an electrode holder that was positioned at a 40 or 90° angle to the craniotomy and controlled by a motorized micromanipulator (MP-225; Sutter Instrument Co.). The obtained electrical signals were amplified with a CV-7B headstage and Multiclamp 700B amplifier, digitized at 10 kHz with a Digidata 1440A and acquired in pClamp (Axon Instruments, Molecular Devices) in parallel with transistor-transistor logic (TTL) pulses from a signal generator (Master-8; AMPI) and with signal from pressure injector system (Toohey Spritzer, Toohey, Fairfield, NJ, USA). Purkinje neurons were identified by the presence of complex spikes followed by a characteristic pause in simple spikes. The cerebellar nuclei contain a high density of neurons that are deeper than and well separated from cerebellar cortical layers, and show clear single unit spike activity. Spike detection was performed using custom code written in MATLAB 2019a.

Histology. Animals were anesthetized with an overdose of ketamine (400 mg/kg)/xylazine (50 mg/kg) (i.p.) and transcardially perfused using a peristaltic pump with phosphate buffered saline (PBS) with 10 mg/ml heparin (Sigma H3149-100KU), followed by chilled 10% formalin (Fisher

Scientific). Brains were extracted from the skull after perfusion, postfixed overnight at 4°C, washed and stored in PBS at room temperature. To visualize the probe locations using the CM-DiI track, brains were cleared and imaged by the BRAIN CoGS histology core facility. All brains underwent the same abbreviated iDISCO+ clearing protocol as previously described (Pisano et al., 2021). In short, after an overnight fix in 4% PFA, brains were rinsed in PBS at room temperature for four 30 minute sessions. Immediately brains were dehydrated 1 hr at each ascending concentration of methanol (20, 40, 60, 80, 100, 100%) and placed overnight in methanol at room temperature. The next day, they were being placed in 66% dichloromethane (DCM)/33% methanol for 3 hrs at room temperature. Brains were cleared with 100% DCM for two 15 min steps then placed in 100% benzyl ether (DBE). Brains were kept in fresh DBE prior to imaging and after for long-term storage. Tissue was imaged using a light-sheet microscope (Ultramicroscope II, LaVision Biotec., Bielefeld, Germany).

For quantification of Purkinje cells, Purkinje cells were stained with calbindin. Animals were transcardially perfused as described above, and after postfixation were stored in PBS at 4°C until sectioning. Whole brain sagittal sections were cut at 90 µm and collected in 0.1 M PBS. Sections were processed for immunohistology by washing with PBS and incubating for 1 hr at room temperature in a blocking buffer (10% normal goat serum, 0.5% Triton in PBS) prior to a 2-day incubation at 4°C in PBS buffer containing 2% NGS, 0.4% Triton and the rabbit anti-calbindin-D-28K primary antibody (C7354; Sigma-Aldrich St. Louis, MO, USA; 1:1000). Sections were subsequently washed in PBS, incubated for 2 hr at room temperature in the PBS buffer with goat anti-rabbit Alexa Fluor 488-conjugated secondary antibody (A-11008; Thermo Fisher Scientific, MA, USA, Invitrogen; 1:400), mounted on glass slides and covered with Vectashield. Images were acquired on the epifluorescent microscope Hamamatsu Nanozoomer. Using NDP.view2 Plus software, individual lobules were identified and Purkinje cells were assigned to lobules for counting.

Corticosterone measurements. Animals were food deprived for 12-24 hrs before blood collection. Immediately after receiving air puffs to whiskers at 20 - 25 psi in a headfixed setup for 10-20 minutes, ~50 µl of blood was collected from the tail vein using a capillary tube, and then immediately disposed of in a heparin-coated 1.5 ml eppendorf tube. Samples were stored on wet ice for maximum 4 hours, after they were centrifuged for 10 mins at 4 ^{o}C at 3000 rpm. Of each

sample 2-10 µl of plasma was collected, placed in new non-coated 1.5 ml eppendorf tubes and stored at -80 ^{o}C. For each animal, two duplicate samples of 1 µl each were used to determine plasma corticosterone levels using the Corticosterone ELISA Kit (K014; Arbor Assays, Ann Arbor, MI, USA) according to the manufacturer's protocol. Plate reading was done using an Infinite 200Pro (Tecan Life Sciences, Morrisville, NC, USA) with i-control software. Results from both duplicates were averaged to get one final corticosterone measurement per animal.

Generalized linear model - hidden Markov model. The generalized linear model - hidden Markov model (GLM-HMM) combines a set of Bernoulli GLMs with a hidden Markov model (Ashwood et al., 2022; Calhoun, Pillow, and Murthy, 2019; Bolkan et al., 2022). For each trial, the animal is modeled to have a latent state that governs its strategy to process information in order to make the binary choice of which side to lick. Each state corresponds to a specific GLM with a unique weight vector of input variables. Between trials, the transition matrix of HMM defines the probability to change from one state to another. The output of GLM-HMM in each trial is calculated as the probability of a Bernoulli reponse (i.e. the probability of a rightward lick) based on both the latent state of current trial and the input variables. Delta cues (Δcues) is the number of air puffs on the right side minus the number of air puffs on the left side. Guide air puffs ('hints') are included. Previous choice 1 is the animal's choice on the previous trial. Previous choice 2 is the animal's choice of the trial prior to the previous trial. Previous reward is the side of the reward on the previous trial. Bias is an offset constant in each state that represents the tendency to lick rightward independent of other input variables. The trials used to calculate the psychometric curve of a latent state are selected to have a posterior probability for that state larger than 0.8. The state occupancy of a certain state is calculated as the fraction of trials whose posterior state probabilities are greatest for that state. The model is trained with the data of 22 wild-type mice on the air puff evidence accumulation task and fitted using expectation–maximization algorithm with code adapted from https://github.com/Brody-Lab/venditto_glm-hmm.

Statistical analysis and presentation. Statistical tests used are indicated throughout the text. All further analysis was done with custom-written code in Python 3 using Spyder (https://www.spyder-ide.org/), and R (https://www.r-project.org/) using RStudio

(https://www.rstudio.com/). For every figure, * = $p \leq 0.05$, ** = $p \leq 0.01$, *** = $P \leq 0.001$. Box and whiskers show median/interquartile range, and 1.5x the interquartile range.

Code and data availability. Code used for data acquisition is available at https://github.com/wanglabprinceton/accumulating_puffs. All data that support the findings of this study will be publicly available upon publication.

576 **Supplemental information**

577 Figure S1 - S7 and Supplementary Table 1 are available for this paper.

578

579 **Correspondence and requests for materials** should be addressed to SW or MO.

580

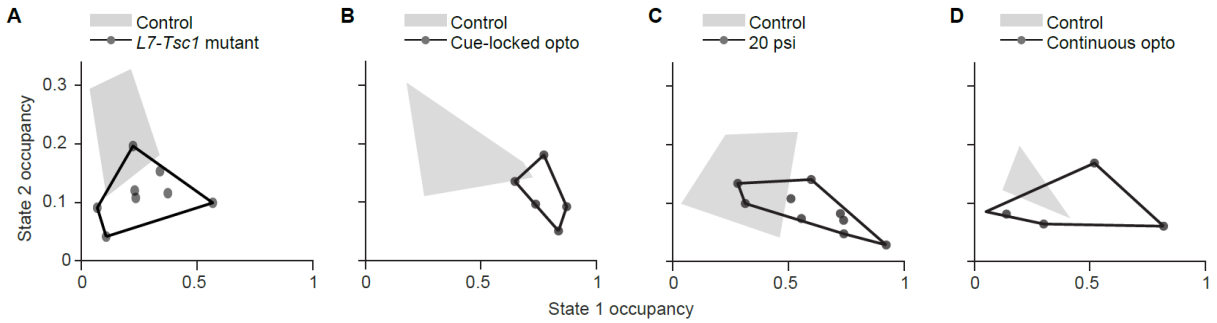

Figure S1 Altered state occupancy occurs already at the earliest levels of manipulation
(A) State occupancy at levels 0, 1, and 2 for *L7-Tsc1* mutant mice. (B) State occupancy at levels 3 and 4 for animals receiving cue-locked optogenetic stimulation of crus I. (C) State occupancy at levels 3 and 4 for animals receiving stronger air puffs (20 psi) to the whiskers. (D) State occupancy at levels 3 and 4 for animals receiving bilateral optogenetic stimulation of crus I during the entire cue period, delay period, and first lick. Shaded areas indicate the area covered by control animals.

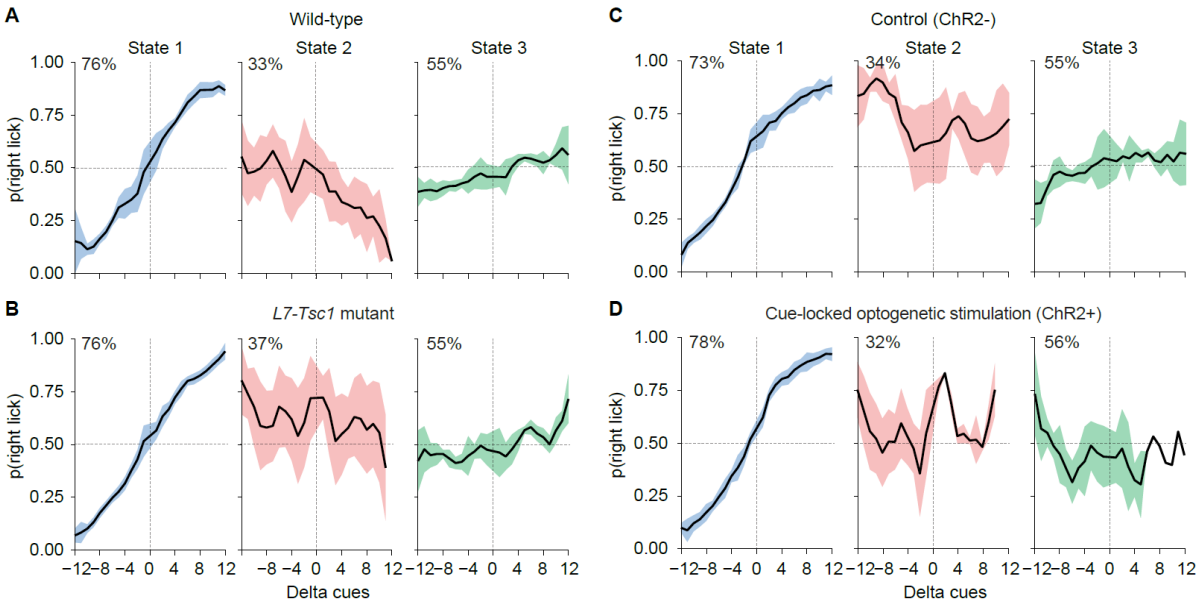

Figure S2 Psychometric curves in the three states remain the same for *L7-Tsc1* mice and for mice receiving cue-locked optogenetic stimulation

(A-D) Psychometric curves for the three states, averaged across all wild-type mice (A), *L7-Tsc1* mutant mice (B), ChR- mice (C) and ChR+ mice receiving cue-locked optogenetic stimulation of Purkinje cells in crus I (D). In the top left of each plot is the percentage correct over all trials in that state. Missing data points or data points without error bars indicate none or one animal at that data point due to low state occupancy. Shaded areas represent 1 s.d.

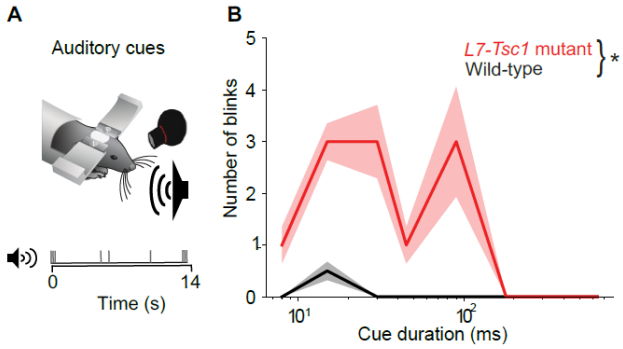

Figure S3 Increased sensory sensitivity in *L7-Tsc1* mice

(A) Schematic of sensory sensitivity tests with auditory cues. (B) Median number of eye blinks in response to auditory cues of different durations for *L7-Tsc1* mutant mice (n = 16) and wild-type littermates (n = 7). A two-way ANOVA indicates an effect of genotype ($F = 5.06$, $P = 0.026$), but not of audio cue duration ($F = 1.697$, $P = 0.11$) or an interaction effect ($F = 0.347$, $P = 0.93$). Shaded areas indicate the estimated s.e.m. using median absolute deviation.

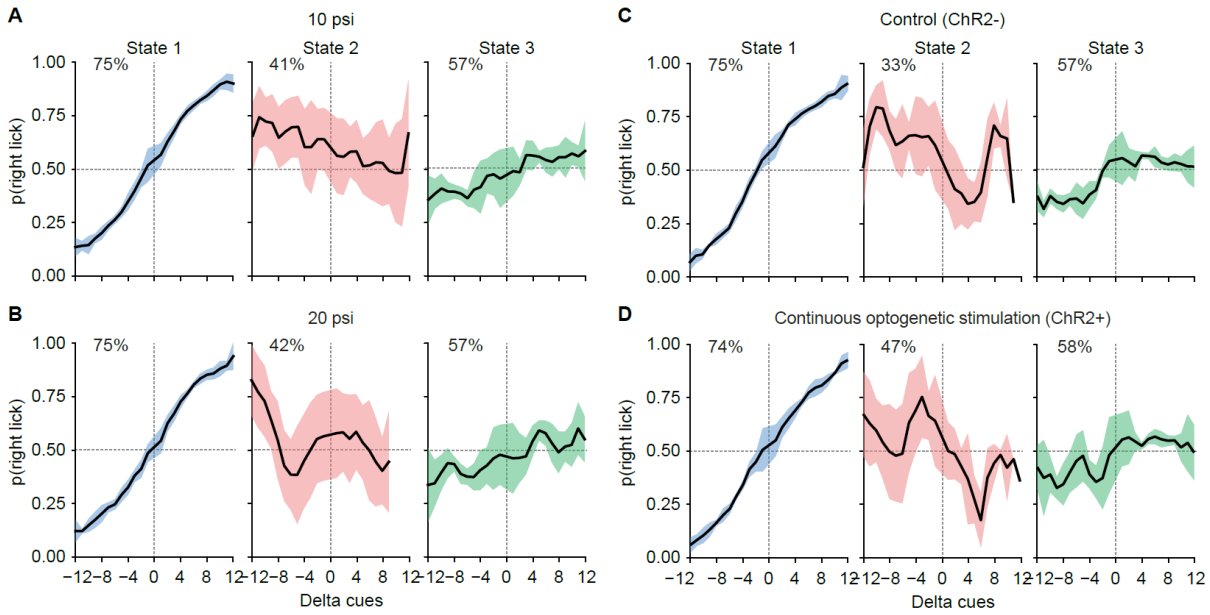

Figure S4 Performance and state occupancy for animals receiving stronger whisker puffs or optogenetic stimulation of Purkinje cells in crus I throughout the entire cue period and delay period

(A-D) Psychometric curves for the three states, averaged across all mice receiving air puffs to the whiskers of regular intensity (10 psi, A) or higher intensity (20 psi, B) or the normal task version for mice not expressing opsin (ChR2-, C) or for mice expressing opsin (ChR2+, D) and receiving continuous optogenetic stimulation to Purkinje cells in crus I during the cue period, delay period, and first lick. In the top left of each plot is the percentage correct over all trials in that state. Shaded areas represent one standard deviation.

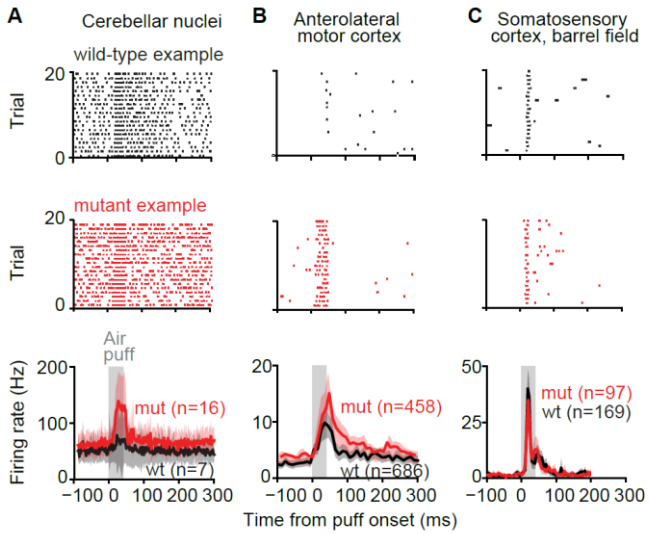

Figure S5 Increased responses to whisker puffs in *L7-Tsc1* mice in cerebellar nuclei and anterolateral motor cortex, but not somatosensory cortex

(A - C) Example raster plots of cerebellar nuclei cells (A), anterolateral motor cortex (B), and the barrel field of the primary somatosensory cortex (C) during 20 trials from *L7-Tsc1* mutants (middle) or their wild-type littermates (top), and average firing rates (bottom) in response to an air puff to the whiskers (data from the same 4 *L7-Tsc1* mutants and 5 wild-type mice as in Figure 3). Shaded areas represent 95% confidence intervals.

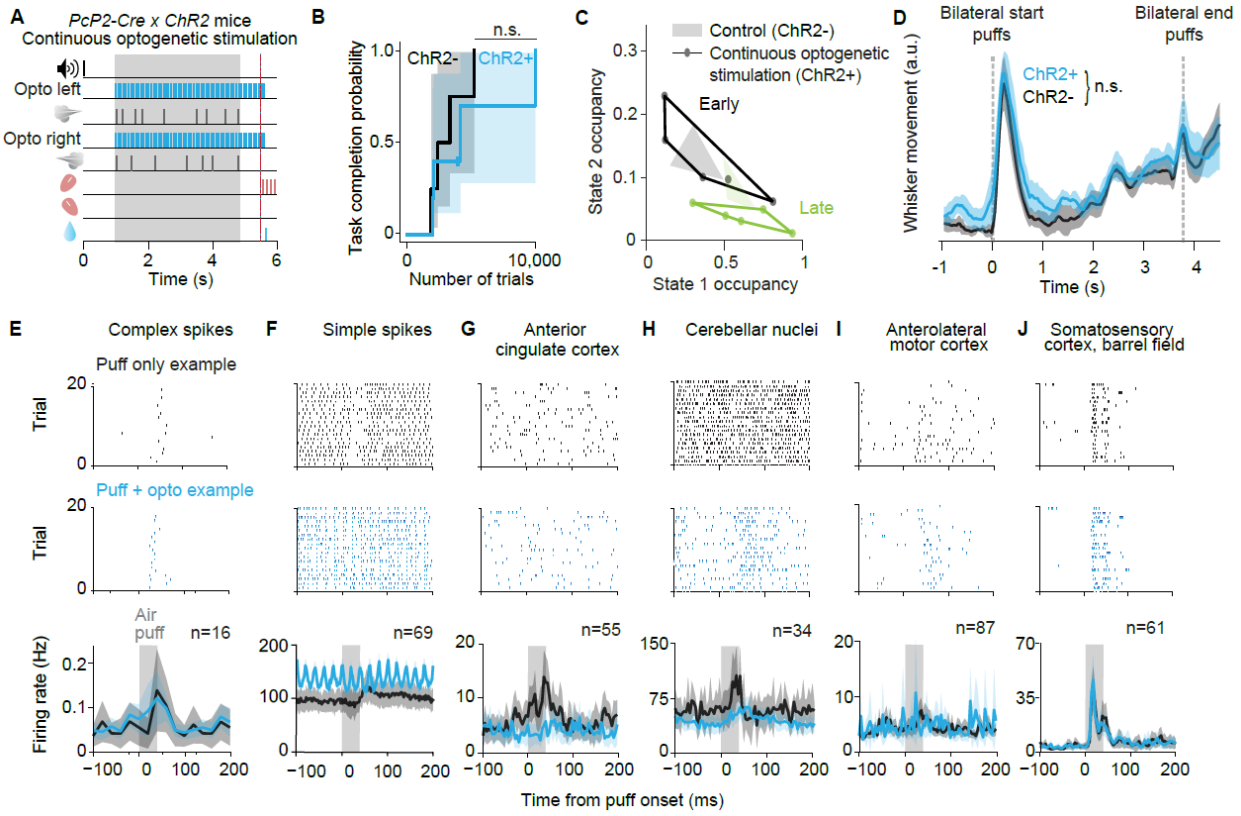

Figure S6 No effect of continuous optogenetic activation of Purkinje cells in crus I on learning of the evidence-accumulation task

(A) Schematic of the evidence-accumulation task with continuous bilateral optogenetic activation of crus I. (B) Kaplan-Meier estimator of task completion probability for *PcP2-Cre* × *ChR2* mice with continuous bilateral optogenetic activation of crus I throughout the evidence-accumulation task (n = 5, median 4210 trials) compared to wild-type littermates (n = 4, median 2534 trials, $\chi^2(1) = 0.31$, $P = 0.33$, log-rank test). (C) State occupancy for mice receiving continuous optogenetic stimulation. Note that the manipulations did only occur in the late levels of the task. Shaded areas indicate the area covered by control animals. (D) Whisker movement during the evidence-accumulation task in response to bilateral whisker puffs at the start and end of each trial. Shaded areas include 95% confidence intervals. (E-J) Example raster plots of: Purkinje cell complex spikes (E), Purkinje cell simple spikes (F) anterior cingulate cortex (G), cerebellar nuclei cells (H), anterolateral motor cortex (I), and the barrel field of the primary somatosensory cortex **(**J) during 20 trials with only a whisker puff (top) or with a whisker puff paired with discounting optogenetic stimulation (middle), and average firing rates in response to an air puff to the whiskers with or without paired optogenetic stimulation of Purkinje cells. Shaded areas represent 95% confidence intervals.

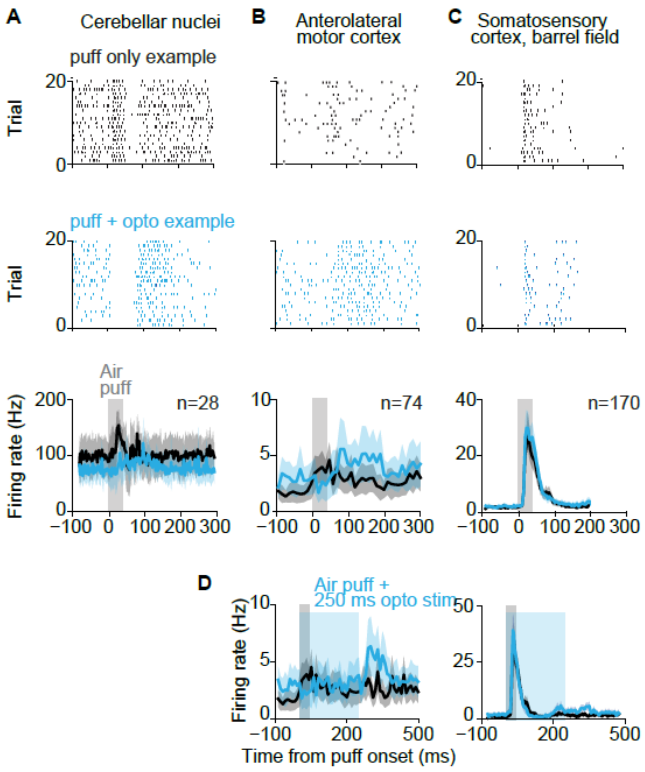

Figure S7 Altered responses to whisker puff and cue-locked optogenetic stimulation of Purkinje cells in crus I in cerebellar nuclei and anterolateral motor cortex, but not somatosensory cortex

(A-C) Example raster plots of cerebellar nuclei cells (A), anterolateral motor cortex (B), and the barrel field of the primary somatosensory cortex (C) during 20 trials with only a whisker puff (top) or with a whisker puff paired with optogenetic stimulation (middle), and average firing rates (bottom) in response to an air puff to the whiskers with or without paired optogenetic stimulation of Purkinje cells. (D) Same as the bottom plots in B and C, but now with a longer duration (250 ms instead of 40 ms) of the optogenetic stimulation. Shaded areas represent 95% confidence intervals.

Supplementary Table 1 | Mice progress through eight different levels during learning of the evidence-accumulation decision-making task.

Level	0	1	2	3	4	5	6	7
Audio cue, 1s before cue period onset	Yes	Yes	Yes	Yes	Yes	Yes	Yes	Yes
Bilateral puffs at start	Yes	Yes	Yes	Yes	Yes	Yes	Yes	Yes
Cue period duration (s)	1	1	1	2.0, 2.8, or 3.8	3.8, or 1.5	3.8, or 1.5	3.8, or 1.5	3.8, or 1.5
Distractor puffs	No	No	No	No	No	No	Yes, 1:9	Yes, 1:4
Bilateral puffs at end	No	No	Yes	Yes	Yes	Yes	Yes	Yes
Delay	200 ms	200 ms	200 ms	200 ms	500 ms	800 ms	800 ms	800 ms
Guide puffs (2.5 Hz) until animal licks	No	Yes	Yes	No	No	No	No	No
Need to lick on correct side for reward	No	Yes	Yes	Yes	Yes	Yes	Yes	Yes
Does first lick need to be correct	No	No	Yes	Yes	Yes	Yes	Yes	Yes
Error trials punished	No	No	Yes	Yes	Yes	Yes	Yes	Yes
Requirements to proceed to next level	15 consecuti-ve rewards	at least 100 trials & 55% correct in window of 40 trials	at least 200 trials & 80% correct in window of 50 trials	at least 100 trials & 75% correct in window of 40 trials	at least 100 trials & 80% correct in window of 40 trials	at least 25 trials & 80% correct in window of 24 trials	at least 250 trials & 75% correct in window of 40 trials	N/A

References

Akrami, A., Kopec, C.D., Diamond, M.E., and Brody, C.D. (2018). Posterior parietal cortex represents sensory history and mediates its effects on behaviour. Nature *554*, 368–372. https://doi.org/10.1038/nature25510.

Ashwood, Z.C., Roy, N.A., Stone, I.R., Urai, A.E., Churchland, A.K., Pouget, A., and Pillow, J.W. (2022). Mice alternate between discrete strategies during perceptual decision-making. Nat Neurosci *25*, 201–212. https://doi.org/10.1038/s41593-021-01007-z.

Badura, A., Verpeut, J.L., Metzger, J.W., Pereira, T.D., Pisano, T.J., Deverett, B., Bakshinskaya, D.E., and Wang, S.S.-H. (2018). Normal cognitive and social development require posterior cerebellar activity. ELife *7*, e36401. https://doi.org/10.7554/eLife.36401.

Bengtsson, F., and Hesslow, G. (2006). Cerebellar control of the inferior olive. The Cerebellum *5*, 7–14. https://doi.org/10.1080/14734220500462757.

Bolkan, S.S., Stone, I.R., Pinto, L., Ashwood, Z.C., Iravedra Garcia, J.M., Herman, A.L., Singh, P., Bandi, A., Cox, J., Zimmerman, C.A., et al. (2022). Opponent control of behavior by dorsomedial striatal pathways depends on task demands and internal state. Nat. Neurosci. *25*, 345–357. https://doi.org/10.1038/s41593-022-01021-9.

Calhoun, A.J., Pillow, J.W., and Murthy, M. (2019). Unsupervised identification of the internal states that shape natural behavior. Nat. Neurosci. *22*, 2040–2049. https://doi.org/10.1038/s41593-019-0533-x.

Carta, I., Chen, C.H., Schott, A.L., Dorizan, S., and Khodakhah, K. (2019). Cerebellar modulation of the reward circuitry and social behavior. Science *363*. https://doi.org/10.1126/science.aav0581.

Chabrol, F.P., Blot, A., and Mrsic-Flogel, T.D. (2019). Cerebellar contribution to preparatory activity in motor neocortex. Neuron *103*, 506-519.e4. https://doi.org/10.1016/j.neuron.2019.05.022.

Chen, X., Du, Y., Broussard, G.J., Kislin, M., Yuede, C.M., Zhang, S., Dietmann, S., Gabel, H., Zhao, G., Wang, S.S.-H., et al. (2022). Transcriptomic mapping uncovers Purkinje neuron plasticity driving learning. Nature *605*, 722–727. https://doi.org/10.1038/s41586-022-04711-3.

Deverett, B., Koay, S.A., Oostland, M., and Wang, S.S.-H. (2018). Cerebellar involvement in an evidence-accumulation decision-making task. ELife *7*, e36781. https://doi.org/10.7554/eLife.36781.

Deverett, B., Kislin, M., Tank, D.W., and Wang, S.S.-H. (2019). Cerebellar disruption impairs working memory during evidence accumulation. Nat. Commun. *10*, 3128. https://doi.org/10.1038/s41467-019-11050-x.

Dombeck, D.A., Khabbaz, A.N., Collman, F., Adelman, T.L. & Tank, D.W. (2007) Imaging large scale neural activity with cellular resolution in awake mobile mice. Neuron *56*, 43–57. https://doi.org/10.1016/j.neuron.2007.08.003.

Frosch, I.R., Mittal, V.A., and D'Mello, A.M. (2022). Cerebellar Contributions to Social Cognition in ASD: A Predictive Processing Framework. Front. Integr. Neurosci. *16*, 810425. https://doi.org/10.3389/fnint.2022.810425.

Fujita, H., Kodama, T., and du Lac, S. (2020). Modular output circuits of the fastigial nucleus for diverse motor and nonmotor functions of the cerebellar vermis. ELife *9*, e58613. https://doi.org/10.7554/eLife.58613.

Gao, Z., Davis, C., Thomas, A.M., Economo, M.N., Abrego, A.M., Svoboda, K., De Zeeuw, C.I., and Li, N. (2018). A cortico-cerebellar loop for motor planning. Nature *563*, 113–116. https://doi.org/10.1038/s41586-018-0633-x.

Garfinkle, J., Guo, T., Synnes, A., Chau, V., Branson, H.M., Ufkes, S., Tam, E.W.Y., Grunau, R.E., and Miller, S.P. (2020). Location and size of preterm cerebellar hemorrhage and childhood development. Ann. Neurol. *88*, 1095–1108. https://doi.org/10.1002/ana.25899.

Happé, F., and Frith, U. (2006). The weak coherence account: detail-focused cognitive style in autism spectrum disorders. J. Autism Dev. Disord. *36*, 5–25. https://doi.org/10.1007/s10803-005-0039-0.

Hatten, M.E. (2020). Adding cognitive connections to the cerebellum. Science *370*, 1411–1412. https://doi.org/10.1126/science.abf4483.

Heijden, M.E. van der, Gill, J.S., and Sillitoe, R.V. (2021). Abnormal Cerebellar Development in Autism Spectrum Disorders. Dev. Neurosci. *43*, 181–190. https://doi.org/10.1159/000515189.

Ito, M. (2006). Cerebellar circuitry as a neuronal machine. Prog. Neurobiol. *78*, 272–303. https://doi.org/10.1016/j.pneurobio.2006.02.006.

Kelly, E., Meng, F., Fujita, H., Morgado, F., Kazemi, Y., Rice, L.C., Ren, C., Escamilla, C.O., Gibson, J.M., Sajadi, S., et al. (2020). Regulation of autism-relevant behaviors by cerebellar–prefrontal cortical circuits. Nat. Neurosci. *23*, 1102–1110. https://doi.org/10.1038/s41593-020-0665-z.

Kennerley, S.W., Walton, M.E., Behrens, T.E.J., Buckley, M.J., and Rushworth, M.F.S. (2006). Optimal decision making and the anterior cingulate cortex. Nat. Neurosci. *9*, 940–947. https://doi.org/10.1038/nn1724.

Kim, O.A., Ohmae, S., and Medina, J.F. (2020). A cerebello-olivary signal for negative prediction error is sufficient to cause extinction of associative motor learning. Nat. Neurosci. *23*, 1550–1554. https://doi.org/10.1038/s41593-020-00732-1.

Klibaite, U., Kislin, M., Verpeut, J.L., Bergeler, S., Sun, X., Shaevitz, J.W., and Wang, S.S.-H. (2022). Deep phenotyping reveals movement phenotypes in mouse neurodevelopmental models. Mol Autism 13, 12. https://doi.org/10.1186/s13229-022-00492-8.

Kloth, A.D., Badura, A., Li, A., Cherskov, A., Connolly, S.G., Giovannucci, A., Bangash, M.A., Grasselli, G., Peñagarikano, O., Piochon, C., et al. (2015). Cerebellar associative sensory learning defects in five mouse autism models. ELife *4*, e06085. https://doi.org/10.7554/eLife.06085.

Küper, M., and Timmann, D. (2013). Cerebellar mutism. Brain Lang. *127*, 327–333. https://doi.org/10.1016/j.bandl.2013.01.001.

Limperopoulos, C., Bassan, H., Gauvreau, K., Robertson, R.L., Sullivan, N.R., Benson, C.B., Avery, L., Stewart, J., Soul, J.S., Ringer, S.A., et al. (2007). Does cerebellar injury in premature infants contribute to the high prevalence of long-term cognitive, learning, and behavioral disability in survivors? Pediatrics *120*, 584–593. https://doi.org/10.1542/peds.2007-1041.

Llinas, R. (2014). The olivo-cerebellar system: a key to understanding the functional significance of intrinsic oscillatory brain properties. Front. Neural Circuits *7*, 96. https://doi.org/10.3389/fncir.2013.00096.

Markram, K., and Markram, H. (2010). The intense world theory – a unifying theory of the neurobiology of autism. Front. Hum. Neurosci. *4*. https://doi.org/10.3389/fnhum.2010.00224.

Mottron, L., Dawson, M., Soulières, I., Hubert, B., and Burack, J. (2006). Enhanced perceptual functioning in autism: an update, and eight principles of autistic perception. J. Autism Dev. Disord. *36*, 27–43. https://doi.org/10.1007/s10803-005-0040-7.

Pachitariu, M., Steinmetz, N., Kadir, S., Carandini, M., and D, H.K. (2016). Kilosort: realtime spike-sorting for extracellular electrophysiology with hundreds of channels. BioRxiv *061481*. https://doi.org/10.1101/061481.

Pellicano, E., and Burr, D. (2012). When the world becomes "too real": a Bayesian explanation of autistic perception. Trends Cogn. Sci. *16*, 504–510. https://doi.org/10.1016/j.tics.2012.08.009.

Pinto, L., Koay, S.A., Engelhard, B., Yoon, A.M., Deverett, B., Thiberge, S.Y., Witten, I.B., Tank, D.W., and Brody, C.D. (2018). An accumulation-of-evidence task using visual pulses for mice navigating in virtual reality. Front. Behav. Neurosci. *12*, 36. https://doi.org/10.3389/fnbeh.2018.00036.

Pisano, T.J., Dhanerawala, Z.M., Kislin, M., Bakshinskaya, D., Engel, E.A., Hansen, E.J., Hoag, A.T., Lee, J., de Oude, N.L., Venkataraju, K.U., et al. (2021). Homologous organization of cerebellar pathways to sensory, motor, and associative forebrain. Cell Rep. *36*, 109721. https://doi.org/10.1016/j.celrep.2021.109721.

Rice, L.C., D'Mello, A.M., and Stoodley, C.J. (2021). Differential Behavioral and Neural Effects of Regional Cerebellar tDCS. Neuroscience *462*, 288–302. https://doi.org/10.1016/j.neuroscience.2021.03.008.

Stoodley, C.J., and Tsai, P.T. (2021). Adaptive Prediction for Social Contexts: The Cerebellar Contribution to Typical and Atypical Social Behaviors. Annu. Rev. Neurosci. *44*, 475–493. https://doi.org/10.1146/annurev-neuro-100120-092143.

Strick, P.L., Dum, R.P., and Fiez, J.A. (2009). Cerebellum and nonmotor function. Annu. Rev. Neurosci. *32*, 413–434. https://doi.org/10.1146/annurev.neuro.31.060407.125606.

Tsai, P.T., Hull, C., Chu, Y., Greene-Colozzi, E., Sadowski, A.R., Leech, J.M., Steinberg, J., Crawley, J.N., Regehr, W.G., and Sahin, M. (2012). Autistic-like behaviour and cerebellar dysfunction in Purkinje cell Tsc1 mutant mice. Nature *488*, 647–651.

https://doi.org/10.1038/nature11310.

Tsai, P.T., Rudolph, S., Guo, C., Ellegood, J., Gibson, J.M., Schaeffer, S.M., Mogavero, J., Lerch, J.P., Regehr, W., and Sahin, M. (2018). Sensitive Periods for Cerebellar-Mediated Autistic-like Behaviors. Cell Rep. *25*, 357-367.e4. https://doi.org/10.1016/j.celrep.2018.09.039.

Wagner, M.J., and Luo, L. (2020). Neocortex-cerebellum circuits for cognitive processing. Trends Neurosci. *43*, 42–54. https://doi.org/10.1016/j.tins.2019.11.002.

Wang, S.S.-H., Kloth, A.D., and Badura, A. (2014). The Cerebellum, Sensitive Periods, and Autism. Neuron *83*, 518–532. https://doi.org/10.1016/j.neuron.2014.07.016.

Yamada, T., Yang, Y., Valnegri, P., Juric, I., Abnousi, A., Markwalter, K.H., Guthrie, A.N., Godec, A., Oldenborg, A., Hu, M., et al. (2019). Sensory Experience Remodels Genome Architecture in Neural Circuit to Drive Motor Learning. Nature *569*, 708–713. https://doi.org/10.1038/s41586-019-1190-7.